

Neutrino Telescope Array Letter of Intent: A Large Array of High Resolution Imaging Atmospheric Cherenkov and Fluorescence Detectors for Survey of Air Showers from Cosmic Tau Neutrinos in the PeV-EeV Energy Range

Makoto Sasaki^{*1} and George Wei-Shu Hou^{†2}

¹ICRR, The University of Tokyo, Kashiwa, Chiba 277-8582, Japan

²Department of Physics, National Taiwan University, Taipei 10617, Taiwan

August 27, 2014

Abstract

This Letter of Intent (LoI) describes the outline and plan for the Neutrino Telescope Array (NTA) project. High-energy neutrinos provide unique and indisputable evidence for hadronic acceleration, as well as a most accurate probe into the hidden sector of traditional astronomy or physics, such as dark matter. However, their extremely low flux and interaction cross section make their detection extraordinarily difficult. Recently, IceCube has reported astronomical neutrino candidates in excess of expectation from atmospheric secondaries, but is limited by the water Cherenkov detection method. A next generation high-energy neutrino telescope should be capable of establishing indisputable evidence for cosmic high-energy neutrinos. It should not only have orders-of-magnitude larger sensitivity, but also enough pointing accuracy to probe known or unknown astronomical objects, without suffering from atmospheric secondaries. The proposed installation is a large array of compound eye stations of imaging atmospheric Cherenkov and fluorescence detectors, with wide field of view and refined observational ability of air showers from cosmic tau neutrinos in the PeV-EeV energy range. This advanced optical complex system is based substantially on the development of All-sky Survey High Resolution Air-shower detector (Ashra) and applies the tau shower Earth-skimming method to survey PeV-EeV ν_τ s. It allows wide ($30^\circ \times 360^\circ$) and deep (~ 400 Mpc) survey observation for PeV-EeV ν_τ s assuming the standard GRB neutrino fluence. In addition, it enjoys the pointing accuracy of better than 0.2° in essentially background-free conditions. With the advanced imaging of Earth-skimming tau showers in the wide field of view, we aim for clear discovery and identification of astronomical ν_τ sources, providing inescapable evidence of the astrophysical hadronic model for acceleration and/or propagation of extremely high energy protons in the precisely determined direction. In this LoI, we present main features of the NTA detector, scientific goal and observational objects, Earth-skimming detection method, the NTA detector, the expected detector performance, and brief summaries of time frame, organization, and funding.

Keywords: Astroparticle physics, Neutrino astronomy, Hadron acceleration, Cosmic ray origin, Dark matter, Gamma ray burst, Active galactic nuclei, Neutrino telescope, PeV-EeV neutrinos, Earth-skimming detection, Tau neutrino, Ashra, Neutrino Telescope Array

^{*}sasakim@icrr.u-tokyo.ac.jp

[†]wshou@phys.ntu.edu.tw

1 Introduction

1.1 Background and Past-related Achievements

High-energy neutrinos uniquely provide indisputable evidence for hadronic acceleration in the universe. High-energy charged cosmic rays have been observed for a long time, but their origin is still a mystery. The energy spectrum follows globally a broken $E^{-\alpha}$ power law, where $\alpha = 2.7 \sim 3.1$, which indicates shock acceleration. Several astronomical object classes have been proposed as potential hadronic accelerators. The galactic and extragalactic magnetic fields prevent us from using the arrival direction observed on Earth to reveal the actual sources. So far, standard astronomical observational data, spanning the electromagnetic wavelengths from radio to γ -ray, have not succeeded in revealing the non-thermal process. On the other hand, high-energy neutrinos should be produced at the accelerators through charged pion production in collisions with radiation fields or the ambient matter, in reactions such as:

$$p + \gamma \rightarrow \Delta^+ \rightarrow \pi^0 + p, \pi^+ + n$$
$$p + \text{nucleus} \rightarrow \pi + X \quad (\pi = \pi^0, \pi^\pm) .$$

Subsequent decay gives the approximate neutrino flavour ratio $\nu_e : \nu_\mu : \nu_\tau = 1 : 2 : 0$ at the sources, which is turned into the ratio of $\nu_e : \nu_\mu : \nu_\tau = 1 : 1 : 1$ by neutrino oscillation upon arrival at Earth. For many astronomical objects, ambient photons are expected to be in the UV region. In that case, the kinetic threshold for photopion production through delta resonance is in the range of several PeV.

The IceCube Collaboration claims the first observation of two PeV-Energy neutrinos, with moderate 2.8σ excess over Monte Carlo expectation of background events [1]. They further extended their analysis to lower energy region [2]. Fitting to the observed photoelectron spectrum, they estimate the diffuse neutrino flux to be $E^2 \phi_{\nu_e + \nu_\mu + \nu_\tau} = 3.6 \times 10^{-8} \text{ GeV sr}^{-1} \text{ s}^{-1}$, assuming an E^{-2} power law flux. The fact that no more events occur in the higher energy region favours neutrinos from astronomical objects but not cosmogenic neutrinos, if the events are true neutrino signals. Assuming astronomical objects where the observed neutrinos were produced, the estimated fluences of the neutrino beams are rather high. It therefore becomes plausible that a next generation high-energy neutrino telescope, with higher sensitivity for high-energy neutrinos and wide field of view, could make clear discovery of hadron accelerators in the Universe.

For cosmogenic neutrinos, produced by the photopion process of protons with the cosmic microwave background, the energy threshold is around $10^{19.6} \text{ eV}$. However, the Pierre Auger Observatory (Auger) claims that heavier components dominate the highest energy region around $10^{19.6} \text{ eV}$ [3]. If true, the flux estimate of cosmogenic neutrinos is much suppressed. Both the cosmic ray flux spectrum around threshold and the density of cosmic microwave background are observed so well, the detection of cosmogenic neutrinos provide a good check of the Auger results on cosmic ray composition. Besides high-energy neutrino detection, the observation of PeV γ -rays could also have provided a clear proof of hadron acceleration, from the subsequent $\pi^0 \rightarrow \gamma\gamma$ decay in the above process. However, in the PeV range, photons are absorbed by interaction with cosmic microwave photons into electron pairs. Therefore, especially if there is good enough pointing accuracy, observation of PeV-EeV neutrinos provide unique and particularly important identification of astronomical cosmic ray origins, as well as examination of cosmogenic neutrino production from extragalactic hadron propagation.

A final answer to the mystery of cosmic ray origins requires the observation of high-energy neutrinos. High-energy neutrinos can be the most accurate probe into hidden sector of traditional astronomy or physics, such as dark matter. However, their extremely low

flux and interaction cross section make their detection extraordinarily difficult. To discover clear, indisputable evidence of cosmic high-energy neutrinos, a next generation detector should have orders-of-magnitude larger sensitivity. To probe into the association with known or unknown astronomical objects as a very high-energy (VHE) neutrino telescope, it should also have enough pointing accuracy, without suffering from background events of atmospheric secondaries.

The Earth-skimming tau neutrino technique enjoys a large target mass by detecting extensive air showers produced by tau lepton decays in the atmosphere. The tau leptons, produced by VHE tau neutrinos that interact with the Earth matter they traverse, emerge out of a mountain or the ground facing the detector. This method has detection sensitivity in the PeV-EeV region, and can be used to search for neutrinos originating from hadron acceleration in astronomical objects. Additional advantages are perfect shielding of cosmic ray secondaries, precise arrival direction determination, and negligible background from atmospheric neutrinos.

The All-sky Survey High Resolution Air-shower detector Phase I (Ashra-1) is an optical-telescope based detector system [4] optimized to detect VHE particles aiming for “multi-particle astronomy” [5, 6]. It is distinguished by two features: (1) an ultra wide optical system in which 42-degree FOV (field of view) is demagnified to 1 inch by using photon and electron optics [7]; (2) high resolution imaging system with trigger. Ashra-1 combines these unique features, resulting in very cost-effective pixels compared to conventional photomultiplier arrays at the focal surface of an optical telescope. Ashra-1 can observe the whole sky with arc minute resolution, with 12 detector units pointing at different directions, where a detector unit consists of a few Light Collectors (LC) pointing at the same direction.

The Ashra-1 detector system is designed so that the focal image is split into trigger/image capture devices after amplification. This feature enables one to simultaneously access 3 kinds of phenomena that have different time scales, i.e., Cherenkov emission (ns), fluorescence (μ s), and starlight (s), without sacrificing the signal to noise ratio. By fully utilizing these distinct features, Ashra aims to undertake full-fledged astronomical observation using VHE particles, commencing with the first detection of VHE neutrinos using Earth and mountain as target [8]. It can also be used to optically observe transient objects like GRBs, as it monitors the whole sky simultaneously [9, 10]. The principal demonstration phase, Ashra-1, has been running at the Mauna Loa site at 3300 m above sea level on Hawaii Island since 2008. The deployed main and sub stations at the Mauna Loa site are shown in Figs. 1 and 2. Ashra-1 succeeded in the first search for PeV-EeV tau neutrinos originating from a GRB in the commissioning run [8], demonstrating the great sensitivity around 100 PeV with the earth-skimming ν_τ technique. Ashra-1 has achieved the best instantaneous sensitivity in the energy region around 100 PeV since January 2012 after trigger upgrade.

The NuTel [11] project, conceived and started in 2001, was an effort concurrent with the development of Ashra-1. It purposed the fast construction of a limited neutrino telescope for detecting ν_τ -originated air showers in the energy range of 1 to 1000 PeV, with possible sources such as AGNs, GRBs, the Galactic Center (GC), etc. It took in the possibility of a base up the smaller Mt. Hualalai, which provides a wide baseline view of Mauna Loa. A MAPMT-based readout electronics, aimed for Cherenkov light in the UV, was quickly built, but the project got cut since 2004. The group still built two 2m telescopes, and conducted a mountain test up 2200 m in Taiwan. But at issue was the estimated event rate of ~ 0.5 events per year, which was not quite convincing. This is where the well developed Ashra-1 comes in contrast: a mature VHE neutrino telescope, which we will call NTA, is at hand.

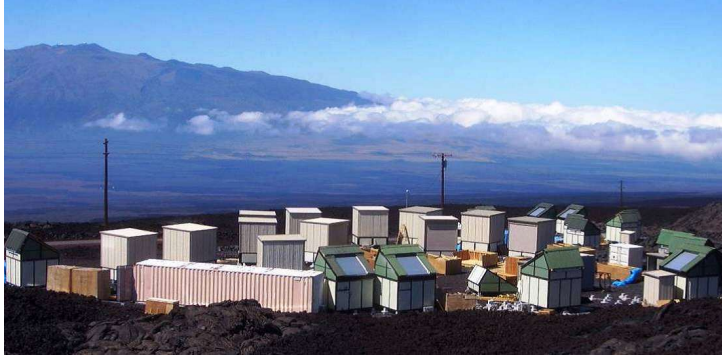


Figure 1: The Ashra-1 main and sub stations at the Mauna Loa site.



Figure 2: A light collector toward Mauna Kea.

1.2 Main Features of the NTA Detector

The key technical feature of the Ashra-1 detector rests on the use of electrostatic lenses, rather than optical lens systems, to generate convergent beams. This enables us to realise a high resolution over a wide field of view. This electron optics requires:

- *wide angle high precision optics* [12]; a Schmidt type optical system with modified Baker-Nunn optics allows a compromise between wide 42° field of view and 1 arc min resolution on the focal sphere of the light collector (Figure 2), with pupil diameter of 1 m;
- *photoelectric lens imaging-tube* [7]; in addition to the optical system, the world's largest imaging-tube uses electrostatic lens to generate convergent beams from photo cathode of 20 inch diameter to output phosphorus window of 1 inch diameter, enabling a very low cost and high performance image sensor that provides high resolution over a wide FOV; and
- *image pipeline* [13]; the image transportation from imaging-tube (image intensifier) to a trigger device and image sensor of fine pixels (CCD+CMOS) with high gain and resolution, enables very fine images with parallel self-trigger systems that trigger for optical flash, atmospheric Cherenkov and fluorescence light separately.

Based on these achievements from Ashra-1, we start to form a new collaboration for realizing the next generation large Neutrino Telescope Array (NTA). The conceptual layout for the NTA observatory considers three site stations for a 25km-side triangle, watching the total air mass surrounded by the mountains of Mauna Loa, Mauna Kea, and Hualalai. A single site station at the center of the triangle has half-sky coverage. This configuration allows for tremendous sensitivity (equivalent to >100 giga ton water), with Cherenkov-fluorescence stereoscopic observation for PeV-EeV neutrinos in essentially background-free conditions. With the demonstrated fine imaging of Earth-skimming tau showers and the significant improved detection solid angle ($30^\circ \times 360^\circ$) for incoming tau neutrinos, we aim for clear discovery and identification of astronomical tau neutrino sources. Also interesting is the unique capability of cross observation between optical flashes, TeV-PeV γ rays, and PeV-EeV ν_τ s, once one or more of these three kinds of self-triggers are observed and associated with an astronomical object.

1.3 Scientific Goal and Observational Objectives

The main scientific goal of the NTA project is:



Figure 3: Layout of the NTA Observatory. Shaded region consists of three semicircles centered at Site1-3.

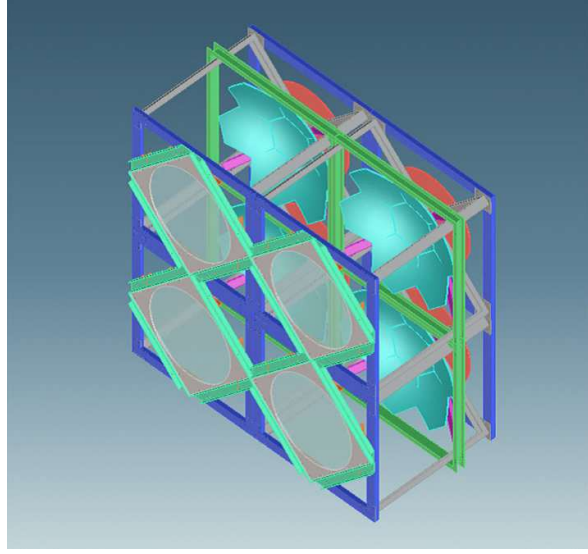


Figure 4: NTA detector unit of four light collectors of the same type.

the clear discovery and identification of non-thermal hadronic process in the Universe.

This has not been directly confirmed by any observation so far and can be achieved by observing PeV-EeV neutrino emission as direct evidence and sensitive probe for collective processes that accelerate particles to energies many orders of magnitude beyond thermal energies.

The following potential candidates are considered as search objectives with the NTA survey, with the sensitive energy range of PeV-EeV (Figure 5).

- Galactic Sources:

Recent calculations show that Super Nova Remnant (SNR) acceleration in our galaxy can describe the whole energy spectrum of observed cosmic rays for the region from TeV up to the ankle, using different types of SNs and transition of composition in the galaxy [14]. Galactic GRBs, which are beamed away from Earth, can be the main source of Galactic cosmic rays at all energies [15]. From the observational point of view, Imaging Air Cherenkov Telescopes (IACTs) have detected more than hundreds of TeV γ -ray sources, including about 30 SNRs [16]. There are three classes of such objects: shell-type supernova remnants, pulsar wind nebulae, and binary systems. The expected neutrino fluxes from these sources and diffuse emission from cosmic ray interaction are calculated [17].

Shell-type Supernova remnants have long been considered as the likely acceleration site for the bulk of the galactic cosmic rays. The morphology of γ -ray emission from RXJ1713.7-3946 was studied [18]. A TeV γ -ray image of the SNR demonstrates that VHE particles are accelerated at the spatially resolved remnant, which has a shell morphology similar to that seen in X-rays. The energy spectrum indicates efficient acceleration of charged particles to energies beyond 100 TeV, consistent with current ideas of particle acceleration in young SNR shocks. Spatial correlations of the γ -ray emission with available target material seem to be present for the SNRs W28, IC443, RCW86 and RX J0852.0-4622 supernova in IACT data. The observations of γ -rays exceeding 10 TeV in the spectrum of the RX J0852.0-4622 supernova [19] has also

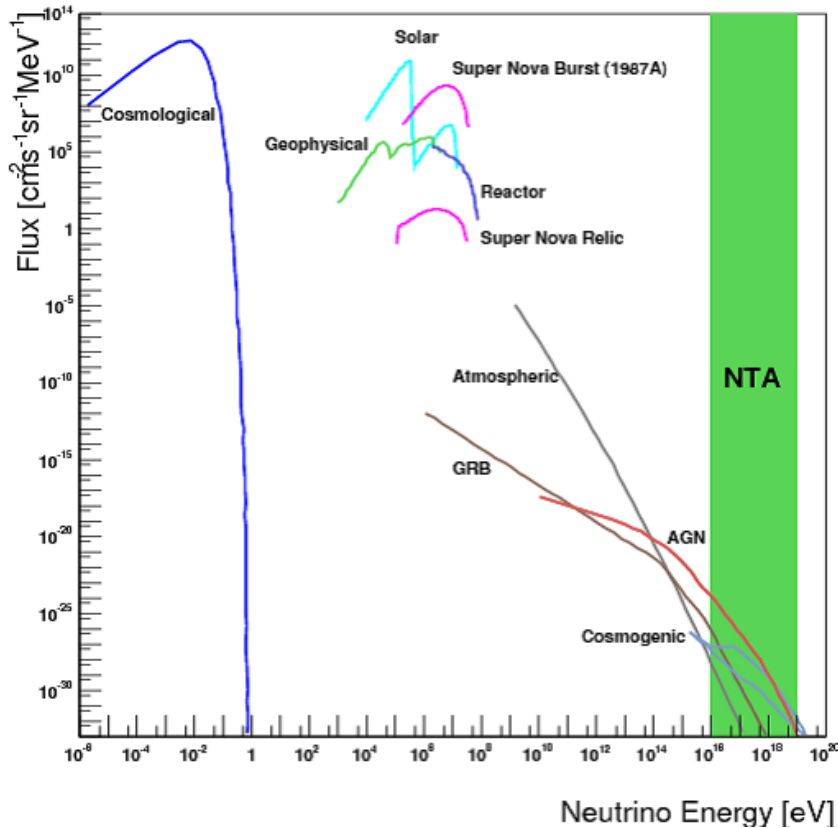


Figure 5: Measured and expected neutrino fluxes, and sensitive energy region of NTA (green band).

strengthened the hypothesis that the hadronic acceleration is the process needed to explain the hard and intense TeV γ -ray spectrum. Such a correlation is also seen in the region of the Galactic Centre (GC). However, in the GC case, the acceleration site of the cosmic rays is not clear [20].

Pulsar Wind Nebulae (PWNe) are some of the brightest TeV γ -ray sources. The central pulsar emits material into the nebulae associated with the powerful Crab and Vela pulsars [21]. A significant fraction of nuclei is suggested to exist in pulsar winds [22]. The decay of pions produced in the interaction of these nuclei can dominate the TeV γ -ray emission, which suggests significant production of neutrinos should occur [23].

Binary systems of a compact object and a massive star are well established galactic TeV γ -ray sources, which are classified into binary PWN or microquasars. In the binary pulsar scenario, the spin-down of the neutron star is the energy source. In the microquasar scenario, accretion is the power-source, and particle acceleration occurs in relativistic jets produced close to the compact object (black hole or neutron star). The PSR 1259-63 system with 3.4-year period and the Be-star SS 2883 belong to the class of binary PWN. LS 5039 and LSI +61 303, are the remaining well established systems and expected as strong neutrino sources [24], of which acceleration site has not been revealed yet. Cyg X-1 is expected as the best γ -ray microquasar candidate, which hosts a black hole [25].

Undetected bright hard-spectrum sources beyond ~ 1 PeV could in principle be missed by current Cherenkov telescopes, since they have substantially reduced energy flux sensitivities in the higher energy region relative to their performance around 1 TeV. Due to the rapid rise of the effective detection area of NTA with energy, such sources could be promising candidates for the NTA detector. Several candidates for sources with hadron acceleration beyond 1 PeV have been identified in the Cygnus region by Milagro [26].

Our Galactic Center (GC) has also been proposed as neutrino sources. An intense diffuse emission of γ -rays with higher energies has been observed which likely implies the presence of a source of cosmic ray protons and thus of neutrinos [20]. The GC region is of particular interest because it is in the good sky view of NTA located on Hawaii Island in the northern hemisphere. A general scenario of Galactic $\gtrsim 10$ PeV cosmic-ray interactions to produce PeV-EeV events [27], and plausible spectra of neutrino events as originating from Galactic cosmic rays [28], has been considered as well. IceCube has announced detection of 26 neutrino events with energies in the ~ 30 -250 TeV range [2], in addition to the two events announced earlier with ~ 1 PeV energy each [1]. The largest concentration of 5 shower-like events detected by IceCube is near the Galactic Center within uncertainties of their reconstructed directions. Adding that, IceCube observed 3 shower-like events which have their arrival directions consistent with the Fermi bubbles [29]. There is an absence of any track-like events in this region. Most of the track-like events are out of the Galactic plane, and at least 4 of them are correlated with shower-like events in those regions [30].

- **Extragalactic Sources:**

As the extragalactic candidates for PeV-EeV neutrino emission, Gamma Ray Bursts (GRB), Active Galactic Nuclei (AGN) and galaxy clusters are well motivated. PeV-EeV neutrinos are also directly linked with the physics of proton acceleration to extremely high energy cosmic rays (EHECR) above EeV at cosmic ray origin objects. Recent measurements of the composition of EHECRs by the Pierre Auger Observatory (Auger) have suggested that the mean nuclear mass may increase with energy between 2 EeV and 35 EeV [3].

Gamma Ray Bursts (GRBs) eject the most energetic outflows in the observed Universe, with jets of material expanding relativistically into the surrounding interstellar matter with a Lorentz factor Γ of 100 or more. Energy dissipation processes involving nonthermal interactions between particles are thought to play an important role in GRBs, but remain observationally unresolved. The detection of PeV-EeV neutrinos (ν s) from a GRB would provide direct evidence for the acceleration of hadrons into the EeV range, and of photopion interactions in the GRB. The GRB standard model [31], which is based on internal/external shock acceleration, has been used to describe the general features of a GRB and the observed multi-wavelength afterglow. However, the standard model cannot reproduce well the recent observational results [32]. The early X-ray afterglows detected by *Swift* exhibit a canonical behavior of steep-flat-steep in their light curve [33]. In some of GRBs, precursor activities were observed [34]. In some cases, the precursor preceded the main burst by several hundred seconds with significant energy emission. To better understand the ambiguous mechanisms of GRBs, observational probes of the optically thick region of the electromagnetic components, as well as hadron acceleration processes throughout the precursor, prompt, and afterglow phases are required. VHE ν s can be used as direct observational probes, which are effective even in optically thick regions. The discovery of nearby low-luminosity

(LL) GRB060218 suggests a much higher local event rate of LL-GRBs [35], which NTA can easily search for. NTA can check the ratio between the observed neutrino event rates from the Earth and the sky in the field of view of the detector, which means the measurement of the diffuse neutrino background from all GRBs with less systematic error.

Active Galactic Nuclei consist of super-massive black holes with $10^6 \sim 10^9$ solar masses in their centre. The black hole radiates huge amount of energy typically of the order of 10^{44} erg/s, which is transferred from gravitational energy after it accretes matter. The energy is expected to induce acceleration of particles. A special class of AGN, Blazars, has jet aligned closely to the line of sight, which can be strong gamma sources. Many sources are reported at GeV and TeV energies in [36] [37]. Gamma ray emission from blazars is often highly variable, e.g. PKS 2155-304, with the most extreme variation observed; an increase by two orders of magnitude within one hour [38]. We should observe the neutrino fluxes from such a source significantly within a short time. An observation of outburst from the blazar 1ES 1959+650 [39] suggests us another type of neutrino sources, which is the TeV emission not accompanied by X-ray emission as synchrotron self-Compton (SSC) models typically predict. A hadronic model does not require TeV emission accompanied by X-ray emission. The observed flares are encouraging sites to search for high energy neutrino emission.

Starburst galaxies have unusually high rates of large-scale star formation processes. A galactic-scale wind is driven by the collective effect of supernova explosions and massive stars at the central regions of the starburst galaxies. IACTs have detected the gamma ray flux at several hundred GeV from the starburst galaxies NGC253 and M82 [40] [41]. They suggest cosmic ray densities much higher than typical case expected in our own Galaxy by two to three orders of magnitude. The diffused neutrino flux from all starburst galaxies is expected detectable with current detectors [42].

Cosmogenic Neutrinos are the secondary particles of the Greisen-Zatsepin-Kuzmin (GZK) process from the interaction of the highest energy cosmic rays with the cosmic microwave background [43, 44, 45]. Various cosmogenic neutrino models (for example [46]) which assume primary cosmic ray protons predict neutrino fluxes. They require 4π solid angle averaged neutrino effective area A_ν to be more than 10^3 km² at 100 PeV to detect several cosmogenic neutrino every year in case of full duty cycle. NTA satisfies this requirement well even assuming the duty of 10%.

- Dark Matter and New Particles

Weakly Interacting Massive Particles (WIMPs) are favoured dark matter candidates, which are preferentially discussed in the minimal supersymmetric standard model (MSSM) framework [47]. Indirect WIMP detection use secondary particles such as γ s, ν s, weak bosons, tau pairs and so on from annihilations. Direct WIMP detection uses recoil nuclei from elastic WIMP-nucleus scattering. There is some complementarity between direct and indirect searches for dark matter, given the astrophysical assumptions inherent to the calculations. Both methods are sensitive to opposite extremes of the velocity distribution of dark matter particles in the Galaxy (low-velocity particles are captured more efficiently in the Sun, high-velocity particles leave clearer signals in direct detection experiments), as well as presenting different sensitivity to the structure of the dark matter halo (a local void or clump can deplete or enhance the possibilities for direct detection). IceCube has evaluated these data for evidence of dark matter annihilations in the Sun, in the Galactic Center, and in the Galactic Halo, searching for an excess neutrino flux over the expected atmospheric neutrino back-

ground, which provides the results of dark matter searches for WIMPs, Kaluza-Klein modes and super heavy candidates (Simpzillas), using the 79-string configurations of IceCube [48]. Given that the Sun is essentially a proton target and that the muon flux at the detector can be related to the capture rate of neutralinos in the Sun, the IceCube limits on the spin-dependent neutralino-proton cross section are currently well below the reach of direct search experiments, proving that neutrino telescopes are competitive in this respect. The simple assumption that dark matter is a thermal relic limits the maximum mass of the dark matter particle, which turns out to be a few hundred TeV for a thermal WIMP, the so called unitarity constraint. However, dark particles might have never experienced local chemical equilibrium during the evolution of the Universe, and their mass may be in the range much larger than the mass of thermal WIMPs, which have been called *WIMPZILLAs* [49, 50]. NTA can perform the most sensitive indirect search for WIMPZILLAs, with much better effective detection area for tau neutrinos from annihilation in the Sun, especially above ~ 10 PeV, the complementary sensitive energy region for IceCube.

Super-heavy particles ($M \gtrsim 10^4$ GeV) produced during inflation may be the dark matter, independent of their interaction strength. Most popular ones are SIMPZILLAs, magnetic monopoles, supersymmetric Q-balls and nuclearites.

Strongly interacting super-heavy particles (SIMPZILLAs) will be captured by the Sun, and their annihilation in the center of the Sun will produce a flux of energetic tau neutrinos that should be detectable by neutrino telescopes [51].

Magnetic monopoles turn out to be consequence of most variants of Grand Unified Theories [52]. The electromagnetic energy losses of monopoles in the atmosphere, as well as neutrinos produced from monopole-antimonopole annihilations in the Sun and Earth, induce clear signatures in optical (Cherenkov and fluorescence) air-shower detectors like NTA [53].

Nuclearites (strange quark matter or strangelets) are hypothetical aggregates of u, d and s quarks, combined with electrons to adjust electric neutrality. Nuclearites, like meteors, produce visible light as they traverse the atmosphere. Their luminosity as a function of their mass is $L = 1.5 \times 10^{-3} (M/1\mu\text{g})$ watt [54]. For example, the apparent visual magnitude of a 20 g nuclearite at a height of 10 km is -1.4 , equal to that of the brightest star, Sirius. Atmospheric nuclearites at galactic velocities ($v \sim 250$ km/s) can easily be distinguished from ordinary meteors bounded to the Solar System, moving no faster than 72 km/s. It could be identified with clear evidence with the wide FOV high resolution optical detector of NTA.

Q-balls are hypothetical coherent states of quarks, sleptons and Higgs fields [55]. Neutral Q-ball (Supersymmetric Electrically Neutral Solitons, SENS) could catalyse proton decay along their path, similar to GUT monopoles. Electrically charged Q-ball (Supersymmetric Electrically Charged Solitons, SECS) would produce light in a similar way as nuclearites.

2 Earth Skimming Tau Neutrino

2.1 Neutrino detection method

To detect VHE neutrinos, a large target volume is required in order to compensate for the very small neutrino-nucleus cross section. On that basis, the secondary particles produced by the first neutrino interaction must be detected in one way or another. The detection method using water and ice as a target detects Cherenkov light from secondary muons,

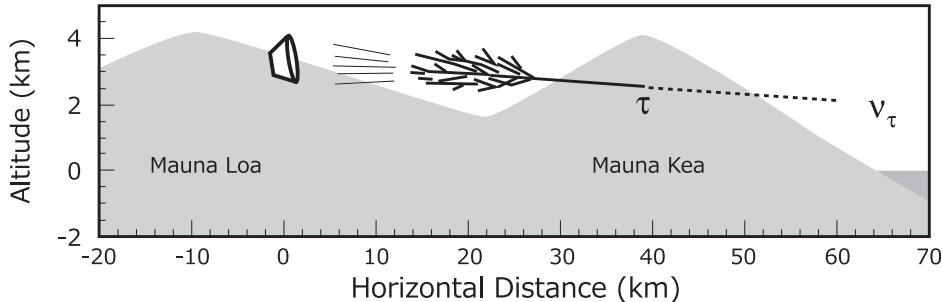


Figure 6: Schematic view of Cherenkov τ shower ES method. Mauna Kea is used as the target mass for neutrino charged current interaction. The produced air shower is observed from Mauna Loa. In addition to the fact that the mountain can be viewed with large solid angle from the observatory, the distance of about 30km from the observatory to the Mauna Kea surface is appropriate for the air shower development, resulting in the huge advantage of the Ashra-1 observatory.

taking advantage of the fact that ice and water are optically transmissive to some extent. This method can be categorized as the method in which the target and detection volumes are identical. On the other hand, the detection method using air showers aims at the detection of higher-energy neutrinos. This method enables us to achieve a huge detection volume as the atmosphere has very high transmittance. However, it is difficult to obtain a larger target mass due to low atmospheric density. The detection method called Earth-skimming ν_τ technique [56, 57, 58, 59, 60] can realize a huge target mass and detection volume at the same time, by dividing the target and detection volume utilizing the interaction process of ν_τ . The detection method is described as follows (see Figure 6). The VHE ν_τ interacts in the Earth or mountain and produces tau lepton (τ). τ penetrates the Earth and/or mountain and appears in the atmosphere. Subsequently, it decays and produces an air shower. Cherenkov photons from the air shower are detected. Owing to the separation of the first interaction where ν_τ produces τ and the τ decay that generates the air shower, air shower observation becomes possible while preserving the huge target mass required for the first interaction. “Cherenkov τ shower ES method” is defined as the detection method which detects Cherenkov photons from tau shower appearing from the Earth or the mountain fully utilizing this feature. We note, for example, that Mauna Kea is over 3,200 km³ in volume and 9.3 tera tons in mass [61].

2.2 Deflection from parent tau neutrinos

This section describes deflection of Cherenkov τ shower compared to the arrival direction of parent ν_τ , in order to estimate the ability to trace back to the accelerator based on the direction of the detected air shower. We evaluate the deflection of the propagating particle in each step of neutrino charged current interaction, τ propagation in the Earth, tau decay, and production of extensive air shower. We use PYTHIA [62] to evaluate neutrino charged current interaction. Since $P_\tau < M_W$ where P_τ denotes the transverse momentum of a produced τ and M_W denotes the mass of the W boson, the deflection angle τ ($\Delta\theta_\tau$) with respect to the parent ν_τ should be less than 0.3 arcmin for $E_\tau > 1$ PeV. The simulation results with PYTHIA are consistent with this.

Second, we use GEANT4 [63] to evaluate the deflection of the τ due to propagation in the Earth. To estimate the energy loss of high energy leptons, the following parametrization

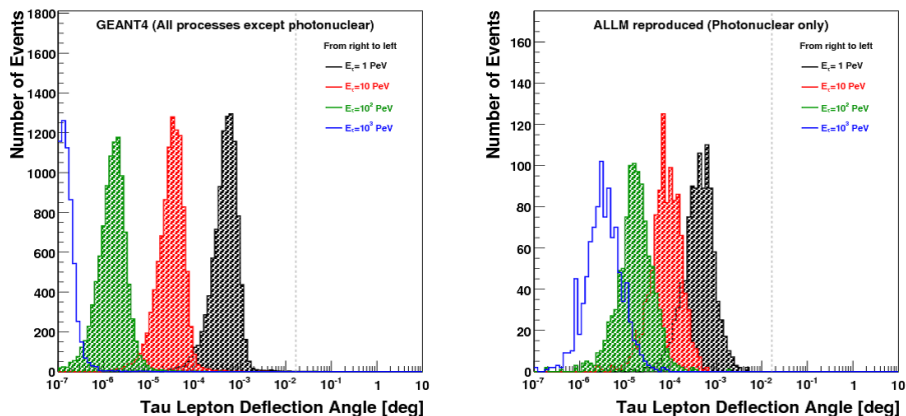


Figure 7: The simulation results of deflection angle of τ s after propagating through 10 km of rock: (*Left*) the GEANT4 result including all high energy processes except for photonuclear interaction; (*Right*) the result of photonuclear interaction from custom simulation. Note that the decay of τ was switched off for the above simulations. The hatched histograms indicate that the τ range is less than 10 km.

is generally adopted [64]:

$$-\left\langle \frac{dE}{dX} \right\rangle = \alpha + \beta E,$$

where α denotes the nearly constant ionization loss, and β denotes the radiative energy loss due to Bremsstrahlung, pair production and photonuclear interaction. Since radiative energy loss is dominant for high energy τ s, these high energy processes must be included in the “Physics List” of GEANT4. Thus, we apply the following processes originally defined for muons to τ s, and estimated the deflection after propagating through 10 km of rock.

- G4MuBremsstrahlung: Bremsstrahlung
- G4MuPairProduction: e^+e^- pair production ¹
- G4MuNuclearInteraction: Photonuclear Interaction

To validate our GEANT4 simulation, we compare the energy dependence of β for Bremsstrahlung, pair production, and photonuclear interaction to Ref. [64]. The β energy dependence agrees well for the former two processes, but we find that GEANT4 produces smaller values for photonuclear interaction at higher energy, and that the difference is a factor of 3 at 10^8 GeV. We write accordingly a toy Monte Carlo simulation for photonuclear interaction using the formalism of Refs. [65, 66], reproducing the energy dependence of β within $\pm 30\%$ accuracy.

Figure 7 shows the simulation results for τ deflection after propagating through 10 km of rock. The left panel shows the GEANT4 result including all high energy processes except photonuclear interaction, while right panel shows our “homemade” simulation result for the latter. These results indicate that photonuclear interaction becomes dominant for deflection at 1 PeV and higher. Note that the decay of τ was switched off for the above simulations, and the hatched histograms indicate that the τ range is less than 10 km. For example, the τ range is 4.9 km at 100 PeV. We conclude that the deflection angle of τ s with energy greater than 1 PeV is much less than 1 arcmin.

¹We modified the original G4MuPairProduction so that momentum conservation includes the produced particles, resulting in the inclusion of deflection.

Next, the deflection due to τ decay is estimated by using the output of TAUOLA [67], taking into account τ polarization. From the mass m_τ , the deflection angle must be less than 1 arcmin if the energy of the secondary particle is higher than 13 TeV. Using TAUOLA output, it was shown that the probability to have deflection greater than 1 arcmin is quite small from the decay of PeV τ s. We conclude that the deflection angle between decay particles which produce the air shower and parent ν_τ is less than 1 arcmin.

Finally, we evaluate the direction of the hadron air shower using CORSIKA. At the shower maximum, we compare the direction of the parent particle (charged pion) to that of electrons and positrons, the dominant producers of Cherenkov photons. We find that the angle between the average direction of electrons and positrons and parent particle of the air shower is coincident within 0.1° at 1 PeV.

In conclusion, we find that the arrival direction of PeV ν_τ s is preserved within 0.1° , including the hadron air-shower generation. The accurate reconstruction of arrival direction by means of fine imaging will be a very powerful technique in the determination of the point sources of PeV ν_τ s.

3 The NTA Detector

The NTA observatory will consist of four sites, Site0, Site1, Site2, Site3, as shown in Figure 3. The conceptual layout for the NTA observatory considers three site stations (Site1, Site2, and Site3) forming a 25km-side triangle watching the total air mass surrounded by the mountains of Mauna Loa, Mauna Kea, and Hualalai. A single site station, Site0, at the center of the triangle has half-sky (extendable to full-sky) coverage. Each site has a centralized group of Detector Units (DU). One detector unit (Figure 4) has a few Light Collecting systems (LC) with segmented mirrors. The features of the system were studied with the Ashra-1 station site constructed on Mauna Loa (3300 m a.s.l.).

In order to investigate the performance of the NTA detector, we shall use the following setup conditions of the assumed locations of observational sites of the NTA system on Hawaii Island.

1. The left side of Figure 8 shows the layout of the NTA site locations. The local Cartesian coordinate system is defined with the origin at Site0, as denoted by “0” in Figure 8, the positive z-axis points to the zenith, and the positive y-axis points north. The x-y coordinates of the site locations are from the projected x-y plane, with the z-coordinates from the corresponding height of the topography data of Hawaii Island.
2. The three observational sites, each located at the vertices of a triangle of equal 25 km side length, are: Site1 at Mauna Loa Ashra-1 location, Site2 on the slope of Mauna Kea, and Site3 on the slope of Hualalai.
3. The central observational site, Site0, is at the center of gravity of the above three site locations. Site1–Site3 are equidistant 14.4 km from Site0.
4. The location of Site1 and Site2 are set at the Ashra-1 Mauna Loa Observation Site (ML-OS), and at 25 km distant from ML-OS in the direction of Kilohana Girl Scout Camp, respectively.
5. After above settings, the locations of remaining two sites are automatically fixed.

The right part of Figure 8 shows the layout of the four sites, superimposed on the topography map image of Hawaii, to be used as settings in the simulation program. Table 1 shows the x-y-z coordinates of the site locations and the detection FOV coverage, as determined from the above description. For the simulation study, given in the next Section, we

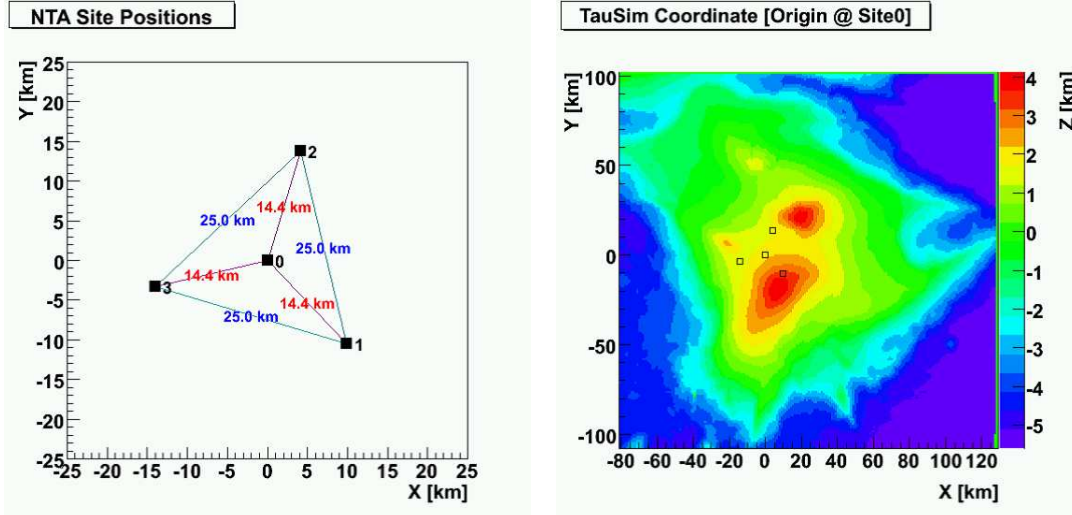


Figure 8: (left) The x-y coordinates of the four NTA site locations, with Site0 defined as the origin; (right) the Hawaii Island topography map superimposed with the four NTA site locations.

Site ID	Location	X [km]	Y [km]	Z [km]	FOV [sr]
Site0	Center	0.000	0.00	2.03	π
Site1	Mauna Loa	9.91	-10.47	3.29	$\pi/2$
Site2	Mauna Kea	4.12	13.82	1.70	$\pi/2$
Site3	Hualalai	-14.02	-3.35	1.54	$\pi/2$

Table 1: The x-y-z coordinates and detection FOV coverage of the four NTA sites, which are used in the simulation program. The location of Site0 is defined as the origin of the coordinate system.

assume that each LC has the total FOV of $32^\circ \times 32^\circ$, trigger pixel FOV of $0.5^\circ \times 0.5^\circ$, and image sensor pixel FOV of $0.125^\circ \times 0.125^\circ$. The Site0 system consists of 12 LCs in the lower elevation angle regions, which together cover the half-sky solid angle that is π sr. The other sites have only 6 LCs in the lower elevation angle region, to cover the FOV of the half-sky solid angle which is $\pi/2$ sr. The bottom edge of the lower elevation angle region is defined to be -9° in elevation angle (9° below the horizon).

Figure 9 shows the simulated panoramic views in altitude and azimuthal directions from the four NTA sites, with colours indicating the distance from the corresponding site.

4 The NTA Detector Performance

We investigate NTA performance with site location setup of previous Section.

4.1 Propagation

For simulating the propagation of ν_τ s and τ s in the Earth, we performed the following procedure and treatment.

1. The density profile of the Earth is chosen according to the Preliminary Earth Model [69, 68]. It depends strongly on the depth in the Earth as shown in Figure 10. We modified the profile just for the density of the ground surface in the radius range of

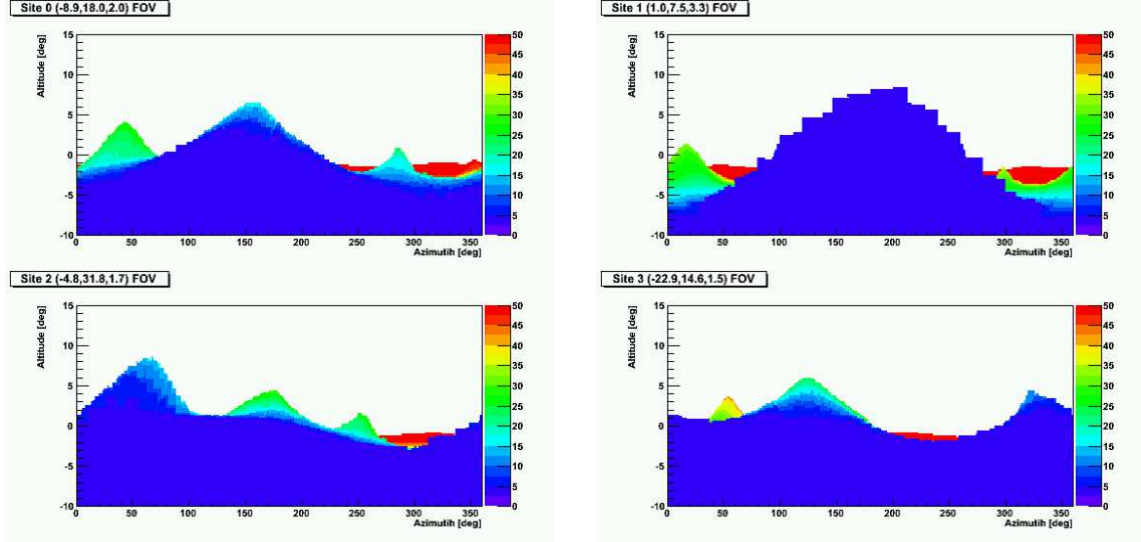


Figure 9: Panoramic views simulating the topographical image from NTA Site0 (top left), Site1(top right), Site2 (bottom left), Site3 (bottom right). Nearby obstacles with distance less than 3 km are neglected.

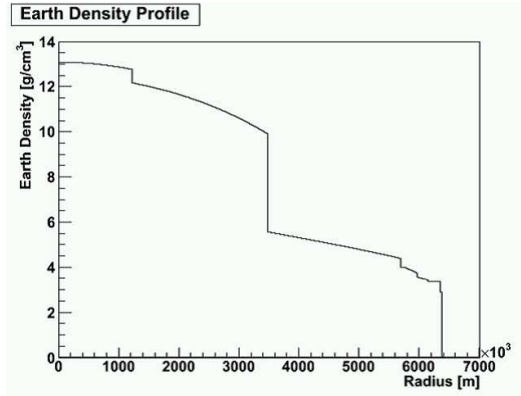


Figure 10: PREM (Preliminary Earth Model) density distribution of the Earth [68]

$r > 6356$ m from 2.6 g/cm^3 into 2.9 g/cm^3 , which is suitable for Basalt rock as the most common type of rock in the Earth's crust and most of the ocean floor around the Island of Hawaii.

2. We took into account both charged current interaction (CC) and neutral current interaction (NC) of ν_τ s and τ s in the Earth. The energy dependence of the inelasticity parameter y for CC and NC based on the CTEQ4 parametrization are shown in [68], and no difference is seen between those for CC and NC.
3. We implement $\nu_\tau \rightarrow \tau \rightarrow \nu_\tau$ regeneration in the simulation. Because of the short lifetime of the tau, regeneration can be an important effect as the ν_τ passes through a significant column depth through the Earth [64].
4. In simulating τ propagation, the current position of τ is evaluated at every step of the energy loss rate of 10%, unless the τ comes out of the Earth or decays.
5. In the lab frame, ν_τ from τ decay on average carries a fraction 0.4 of the τ energy [70]. We used this constant average value of 0.4 as the energy of ν_τ from τ decay, without

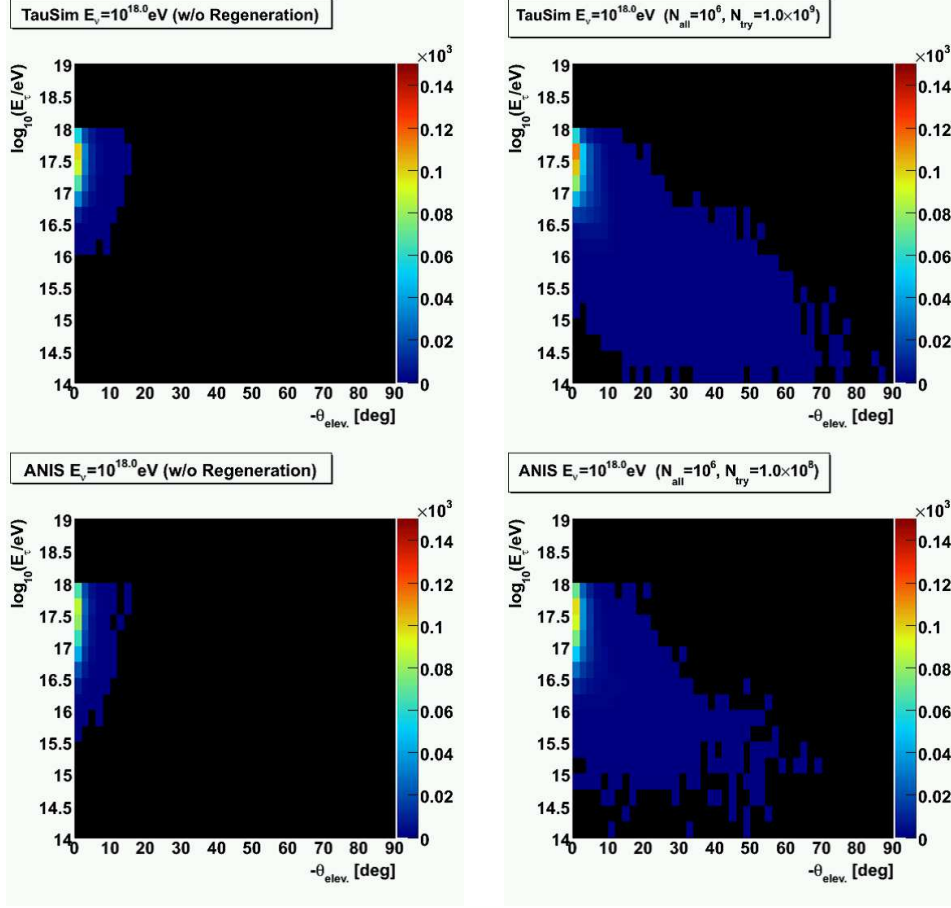


Figure 11: Distribution in the E_τ and dip angle (minus elevation angle; $-\theta_{elev}$) plane in the case of primary ν_τ energy of 10^{18} eV.

taking into account the energy distribution. The error from this approximation can be neglected for the moment, because of the good agreement between results with our simulation and with ANIS (All Neutrino Interaction Simulation) [71], as shown in Figure 11.

Figure 11 (top) shows the distribution in the plane of E_τ and dip angle (minus elevation angle; $-\theta_{elev}$) in the case of primary ν_τ energy of 10^{18} eV.

The left side shows the case of neglecting any effect from $\nu_\tau \rightarrow \tau \rightarrow \nu_\tau$ regeneration or NC interaction of ν_τ in the Earth, while the right side shows the case of taking into account both effects from $\nu_\tau \rightarrow \tau \rightarrow \nu_\tau$ regeneration and NC interaction of ν_τ in the Earth. Each bin content in these figures is given by:

$$\frac{d^2 N_\tau}{dE_\tau d\Omega}(E_\tau, \theta) \times d \log_{10} E_\tau \cdot 2\pi d\theta.$$

Figure 11 (bottom) shows the result using ANIS [71], which is approved for use for AMANDA and IceCube, and acknowledged well for detailed interactions, decays, and propagation of ν_τ s and τ s. In general, the results with our simulation and ANIS agrees reasonably well. From detailed comparison, we should consider systematic errors of $\sim 12\%$ on produced τ flux in the Earth in using our simulation program.

4.2 Simulation

Before evaluation of the performance of NTA using our simulation program, we summarize our settings at the following three steps.

1. Simulation for the Earth-skimming $\nu_\tau \rightarrow \tau$
 - ν_τ (CTEQ4) [72]
 - Inelasticity parameter [68]
 - Energy loss in the Earth [64, 73]
2. Air-shower simulation: $\tau \rightarrow$ Cherenkov and fluorescence light
 - τ Decay (approximated; [74])
 - Air-shower generation (Gaisser-Hillas + NKG) [74]
3. Detector simulation:
 - light collection and throughput of light
 - simplified triggering logic
 - Event reconstruction is not implemented yet.

We assume the following input parameters.

Light Collection Area: $A = 7.07 \text{ m}^2$ (equivalent with the effective pupil diameter of $\phi 3 \text{ m}$)

Optical filter transmittance: $\epsilon_{\text{flt}} = 90\%$

Quantum efficiency of photoelectric tube: $\epsilon_{\text{QE}} = 24\%$

LC FOV: $32^\circ \times 32^\circ$

Trigger pixel FOV: $0.5^\circ \times 0.5^\circ$ / trigger pixel

Exposure time in trigger pixel: $t_{\text{trigpix}} = 50 \text{ ns}$

Required trigger condition:

To estimate the detection sensitivity of NTA the event candidates must satisfy the following requirements:

- total number of photoelectrons detected in one LC must satisfy:

$$N_{\text{pe}}^{\text{LC}} > 61,$$

- S/N estimated in the track-associated box of the width of 4 pixels and the length of 64 pixels, which includes the candidate event air-shower track, must satisfy:

$$S/N > 4,$$

where the standard deviation of night sky background in the track-associated box with the exposure of 50 ns is estimated as $\sigma(N_{\text{pe}}^{\text{BG}}) = 15.4 \text{ pe}$ from a night sky background estimate [75] given by $2.0 \times 10^5 \text{ photons/m}^2/\text{sr}/\mu\text{s}$.

A simulated Earth-skimming τ shower event with primary ν_τ energy of $E_\nu = 10^{17} \text{ eV}$ using the above settings is shown in Figure 12. The reconstructed air-shower axis with simple fits to the Cherenkov and fluorescence hit map images taken by the two sites reproduces the primary ν_τ arrival direction with an error of 0.08° .

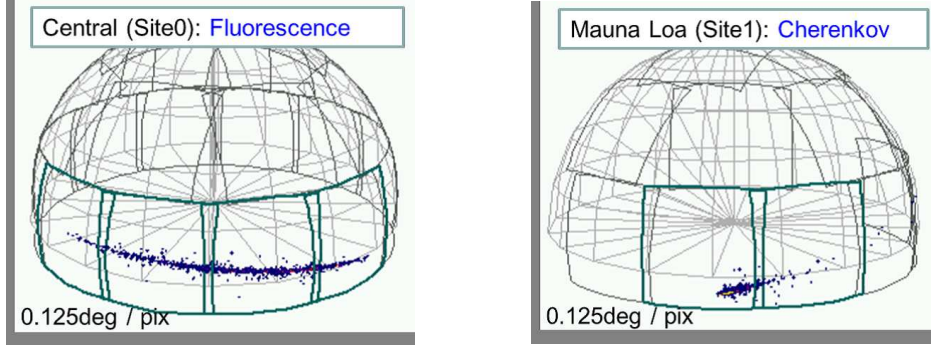
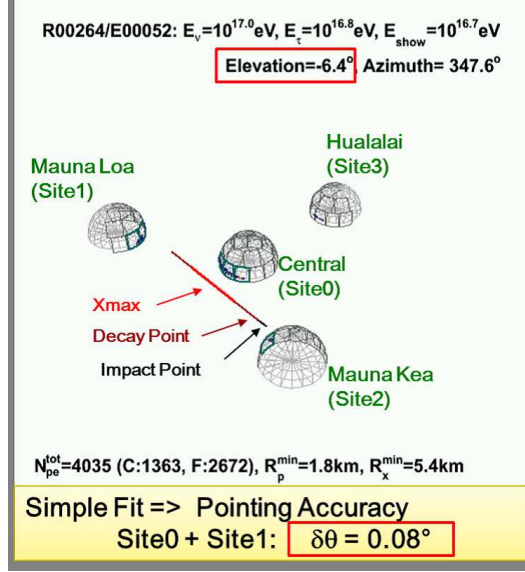


Figure 12: A simulated Earth-skimming τ shower event with primary $E_{\nu_\tau} = 10^{17} \text{ eV}$, which has both fluorescence image taken by Site0 and Cherenkov by Site1. (top) Global hit map view in the NTA system; (bottom left) air-shower fluorescence image taken by Site0, and (bottom right) Cherenkov image from the same event taken by Site1. The trigger pixel and fine image FOVs are $0.5^\circ \times 0.5^\circ$ and $0.125^\circ \times 0.125^\circ$, respectively.

ν_τ Energy	CTEQ4 σ_{CC}	L_{CC}	θ_{elev}^c
10^{15} eV	$6.342 \times 10^{-34} \text{ cm}^2$	$2.62 \times 10^9 \text{ g/cm}^2$	-30.6°
10^{16} eV	$1.749 \times 10^{-33} \text{ cm}^2$	$9.49 \times 10^8 \text{ g/cm}^2$	-13.0°
10^{17} eV	$4.436 \times 10^{-33} \text{ cm}^2$	$3.74 \times 10^8 \text{ g/cm}^2$	-5.71°
10^{18} eV	$1.049 \times 10^{-32} \text{ cm}^2$	$1.58 \times 10^8 \text{ g/cm}^2$	-2.45°
10^{19} eV	$2.379 \times 10^{-32} \text{ cm}^2$	$6.98 \times 10^7 \text{ g/cm}^2$	-1.08°

Table 2: Based on CTEQ4 [72], differential ν_τ CC cross section (σ_{CC}), corresponding interaction length (L_{CC}), and the critical angle (θ_{elev}^c) such that the chord thickness at the critical angle corresponds to L_{CC} . For the Earth density profile, we refer to the parametrization of PREM [68, 71].

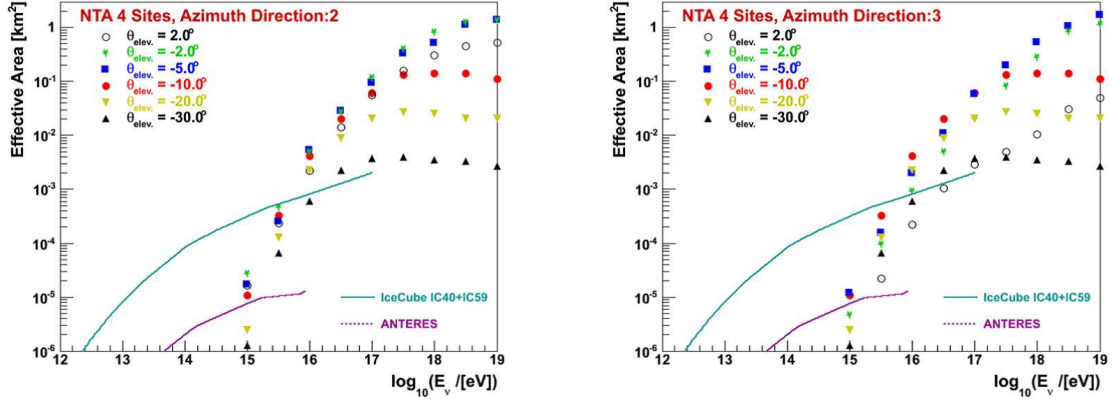


Figure 13: Estimated effective detection area simulated for ν_τ from a point source with azimuthal arrival direction corresponding to (left) Mauna Loa (ϕ_2) and (right) Hualalai (ϕ_3) with respect to the central site of Site0, and dip angles of 2.0° (black open circle), -2.0° (green star), -5.0° (blue filled box), -10.0° (red filled circle), -20.0° (yellow filled triangle), and -30.0° (black filled triangle).

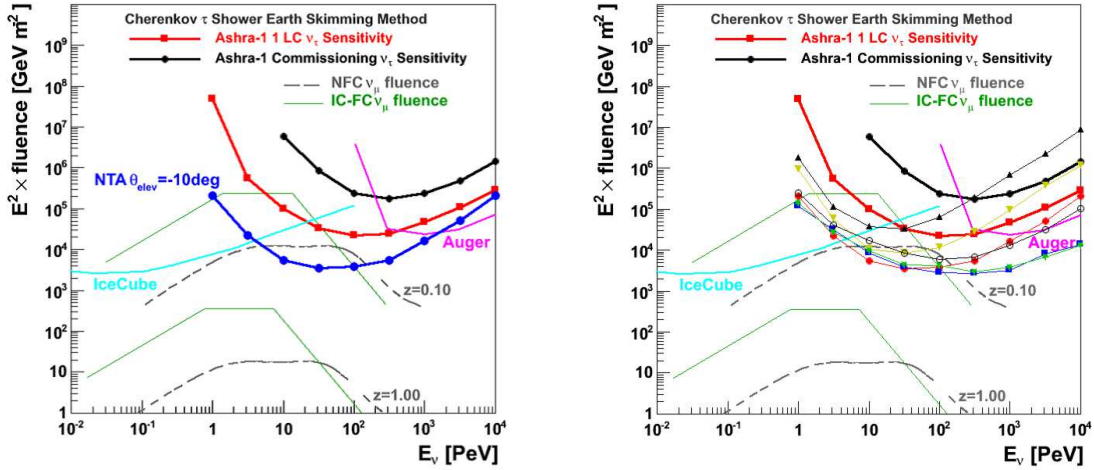


Figure 14: Comparison of differential sensitivities as function of E_{ν_τ} for a point source of ν_τ , calculated as the Feldman-Cousins 90% CL limit event number for null expected events, using a light collector (LC) from Ashra-1 commissioning [8], one Ashra-1 LC design, the NTA layout of LCs, in the cases of (left) $\theta_{\text{elev}} = -10^\circ$, (right) $\theta_{\text{elev}} = +2^\circ$ (opencircle), -2° (green), -5° (blue), -10° (red), -20° (yellow), and -30° (black). The sensitivities published from IceCube [76] and Pierre Auger Observatory [77] are shown, as well as theoretical estimates used for the former (solid lines) and recalculated by Hümmer et al. (dashed lines) [78] assuming the distance of $z \sim 0.1$ and 1.0 .

4.3 Sensitivity

We estimate the effective detection area for ν_τ fluence from a point source with our simulation program for Earth-skimming τ showers incorporating the appropriate Earth model [69], the topography around the NTA observatory, the interaction and propagation process of ν_τ and τ in the Earth [68, 71], the decay of τ and generation of air-shower, with parameter choices as described before.

We define the critical dip angle (minus critical elevation angle; $-\theta_{\text{elev}}^c$) as the chord thickness at the dip angle $-\theta_{\text{elev}}^c$ that corresponds to the CC interaction length $L_{\text{CC}}(E_\nu)$, determined by the interaction cross-section $\sigma_{\text{CC}}(E_{\text{CC}})$ for a ν_τ traveling with energy E_ν . Table 2 shows differential cross sections of ν_τ CC interaction σ_{CC} based on CTEQ4 [72], the corresponding interaction length L_{CC} , and θ_{elev}^c for each E_{ν_τ} between 1 PeV and 10 EeV.

Taking into account the critical dip angles for the energies of ν_τ in Table 2, we estimated the effective detection areas for ν_τ from a point source with azimuthal arrival direction corresponding to that of the Mauna Loa summit (ϕ_2) and that of the Hualalai summit (ϕ_3), with respect to the central site of Site0, and dip angles of 2.0° , -2.0° , -5.0° , -10.0° , -20.0° , and -30.0° , as shown in Figure 13.

Figure 14 shows the differential sensitivities, as a function of E_{ν_τ} for a point source of ν_τ , calculated as in [79] requiring 2.3 events in a bin size of one energy decade $\Delta \ln E_\nu$. The 2.3 events is the Feldman-Cousins 90% CL limit event number for null expected events.

Figure 15 (top) shows the diffuse sensitivities for ν_τ fluxes with NTA for 3 year observation time. Both differential and integral sensitivities are given. The sensitivity limit is defined as $2.3E_\nu/(S\Omega_{\text{eff}} \cdot \Delta T)$. Also shown is the comparison between NTA, Pierre Auger Observatory [77] and IceCube [80]. The bottom figure shows essentially the same plots as the top one, but various model predictions for cosmogenic ν s as well as other experiments of RICE, AMANDA, and ANITA are superimposed [81]. For the diffuse sensitivities of NTA, we assume the duty of 10% for 3 years observation ($\sim 9.5 \times 10^6$ s) and trigger conditions as described before.

4.4 Exposure

From Figure 13, NTA can survey ν_τ point sources with best sensitivity in detection solid angle for ν_τ defined as $-30^\circ < \theta_{\text{elev}} < 0^\circ \times 0^\circ < \phi_{\text{azi}} < 360^\circ$ in the primary ν_τ energy region of $10 \text{ PeV} < E_{\nu_\tau} < 1 \text{ EeV}$. From Figure 14, the survey depth can be better than redshift $z < 0.1$ corresponding to a distance of ~ 400 Mpc.

With the observational conditions assumed as follows:

- Solar elevation angle: $< -18^\circ$
- Lunar bright surface ratio: < 0.2
- Ideal weather efficiency: 100%

the total duty is estimated to be 20.5%, which corresponds to maximum observation time of 1800 hours per year.

Figure 16 shows the exposure map for the observation with NTA on Hawaii Island (the Site1 position: $19^\circ 32' 28''$ N, $155^\circ 34' 03''$ W, 3294 m a.s.l.), with Mollweide projection in Galactic (left) and Equatorial (right) coordinates on the celestial sphere. The maximum observation time is normalized to 1000 hours per year, as shown in red in the figure where NTA can detect with maximum efficiency, which means total duty of 11.4%, corresponding to about half the above ideal case. The location of NTA on Hawaii Island allows us to enjoy a survey of our galactic center for more than several hundred hours each year.

4.5 Effect of Changing Site Layout

To check the effect of changing the site layout on the detection sensitivity of NTA, we changed only the location of Site0 into the midpoint between Site2 and Site3, as shown in Figure 17 (left), and repeated the sequence of simulation for diffuse sources as before. The right side of Figure 17 shows the ratio of the two sets of effective detection area for ν_τ s as

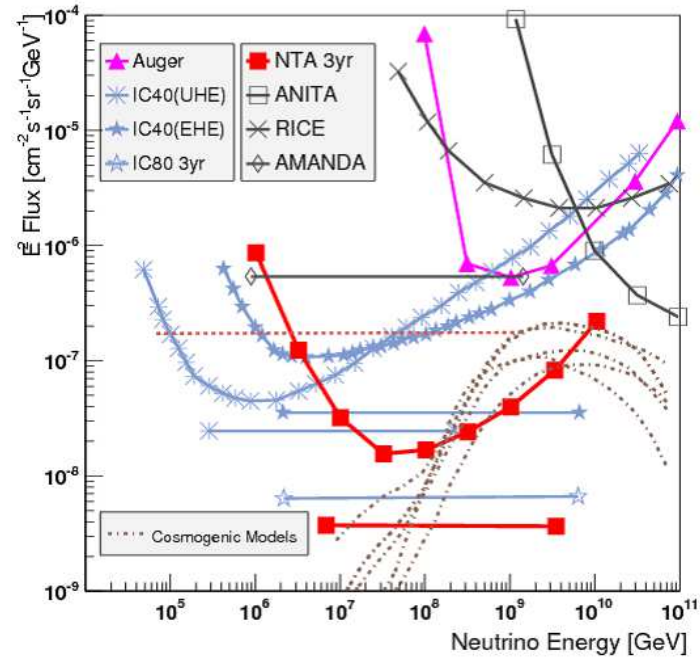
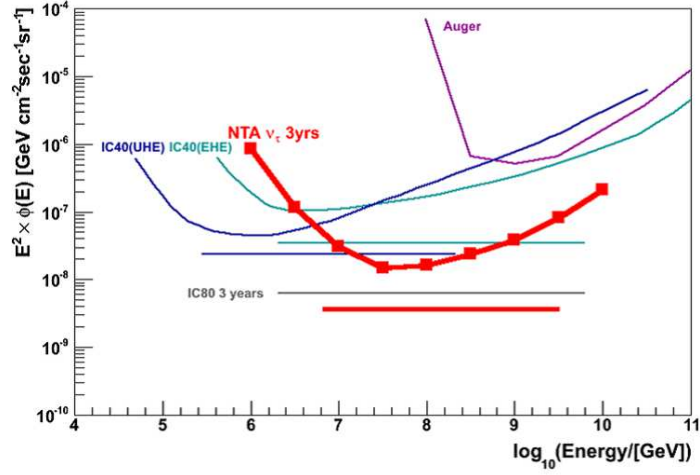


Figure 15: Diffuse sensitivities for ν_τ fluxes with NTA for 3 years observation time. Both differential sensitivity (curve) and integral sensitivity assuming the E^{-2} flux spectrum (horizontal line) are shown. The sensitivity limit is defined as $2.3E_\nu/(S\Omega_{\text{eff}} \cdot \Delta T)$. Comparison among NTA, Pierre Auger Observatory [77] and IceCube [80]. (bottom) essentially the same as the top one but various model predictions for cosmogenic ν s as well as other experiments of RICE, AMANDA, and ANITA are superimposed [81]. For NTA, the duty of 10% for 3 year observation ($\sim 9.5 \times 10^6$ s) is assumed.

a function of E_{ν_τ} , which are obtained with modified layout and regular one. We do not see any significant change over all energies in the PeV-EeV region. The layout can therefore be adapted to practical concerns.

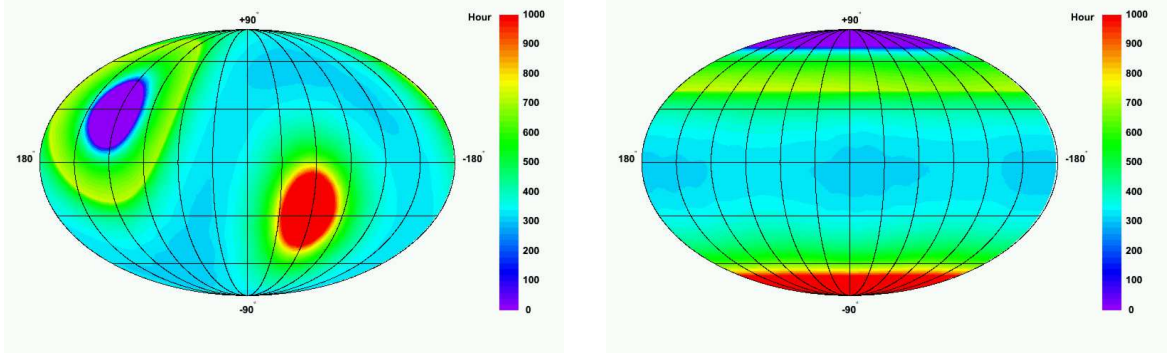


Figure 16: Exposure map for observation with NTA on Hawaii Island (the Site1 position: $19^{\circ}32'28''$ N, $155^{\circ}34'03''$ W, 3294 m a.s.l.), with Mollweide projection in Galactic (left) and Equatorial (right) coordinates. Maximum observation time is normalized to 1000 hours per year (red), where NTA can detect with maximum efficiency (total duty of 11.4%).

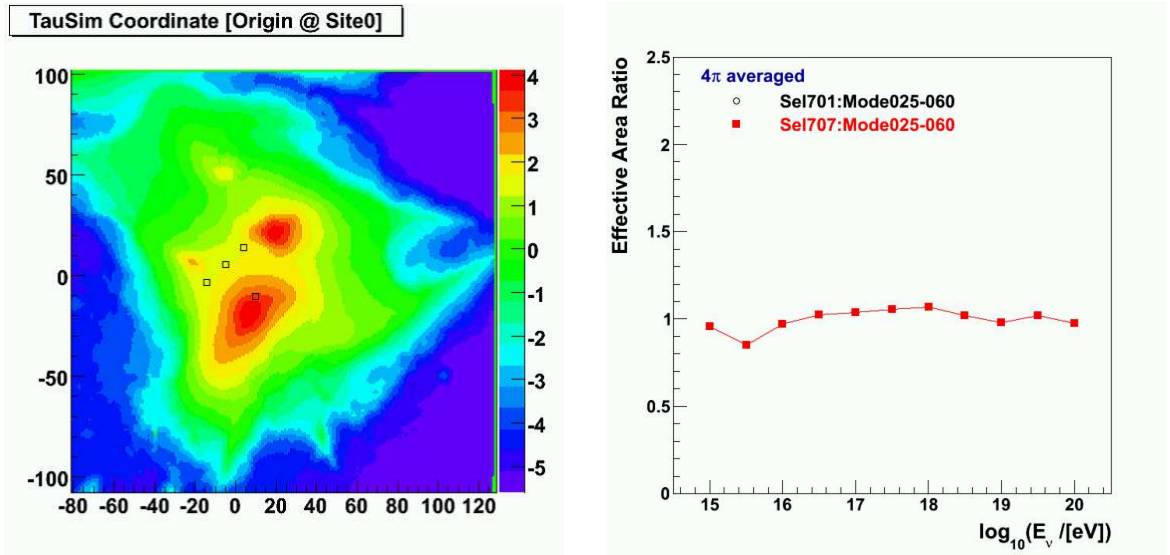


Figure 17: (left) Modified layout of NTA sites, and (right) ratio of the two sets of effective detection area for ν_{τ} s as a function of $E_{\nu_{\tau}}$, obtained with modified and regular layouts (Figure 8). The location of Site0 is changed into the midpoint between Site2 and Site3.

4.6 Angular resolution [82]

As discussed in Section 2.2, a Cherenkov τ shower with $E > 1$ PeV preserves the arrival direction of the parent ν_{τ} to within 0.1° accuracy. This means that the ability of the detector to reconstruct the arrival direction results in the precise identification of the VHE neutrino sources and leads to the realization of “multi-particle astronomy”. Owing to its high-resolution imaging capability, the NTA detector has a huge potential to improve the reconstruction of the arrival direction of ν_{τ} -induced air showers. In this subsection, shower reconstruction with likelihood analysis will be discussed, where simulated air-shower images are generated with faster Gaisser-Hillas and NKG parametrization [74], which are well established [83, 84].

The shower axis direction (n_x, n_y) in the obtained fine image and intersection of mountain surface with shower axis (tau emerging point) projected onto the obtained image (X', Y')

determine the geometric relationship between the detector and the shower axis, and therefore the impact parameter (R_P). Easy and direct comparison between real and simulated data was attained by adopting the positions in the obtained image as the parameters for event reconstruction. The positions in the obtained image correspond to the directions in the light collector's FOV. For investigation of the reconstruction capability, we simulated a 10 PeV proton shower incoming at a zenith angle of 65° . For this type of event, the definition of (X', Y') has to be different. We took the intersection of 25 km height with the shower axis projected into the obtained image as (X', Y') .

The following geometrical reconstruction parameters are taken as a typical shower example to study the reconstruction accuracy:

- $(n_x, n_y) = (0.0, 0.0)$ [deg];
- $(X', Y') = (0.6, 0.0)$ [deg];
- $E = 10$ [PeV].

This parameter set corresponds to $R_P = 540$ m. To generate the shower images, the longitudinal and lateral developments of air shower are calculated using Gaisser-Hillas and NKG, respectively. The direction of Cherenkov photon is calculated by using the parametrization described in Ref. [85], where normalization is adjusted to reproduce the R_P dependence of the detected number of photoelectrons (N_{pe}) obtained with CORSIKA. We confirm that the R_P dependence is reproduced within $\pm 15\%$ within the R_P range we use in this study. In this simulation, fluctuation due to the first interaction point is taken into account, but air-shower fluctuation due to hadron interaction is not. This effect is accounted for in Section 2.2 (0.1° at 1 PeV). Although it is preferable to include hadron air-shower fluctuation using CORSIKA, generating a sufficient number of events is too demanding on CPU power.

Considering the fact that X' determines R_P , strong correlation between n_x and R_P results in a worse joint resolution. This is a well-known problem connected with the mono detection of Cherenkov shower and is greatly improved in case of stereo detection with multiple light collectors. Since the maximum likelihood method uses the slope of the probability density distribution, it is important to include the night sky background (NSB) photoelectrons. NSB photoelectrons were added as a probability per pixel in probability density distribution.

We estimate the region for which the likelihood is calculated by using each “dummy real data” by defining cut positions which correspond to 5% of the peak in the projections of major and minor axes. In the major and minor axis projection, we use asymmetric and symmetric Gaussians to fit their shape, respectively, and calculate the 5%-peak positions to reduce the effects of statistical fluctuation toward the tails of the distributions. After selecting (n_x, X') which gives minimum L in each “dummy real data”, the distribution of residuals between the reconstructed and true directions (Δn_x ; defined as reconstructed minus true positions in the obtained image) is obtained.

We use a *Length* cut parameter (ℓ_{cut}) as the estimator of R_P , where ℓ_{cut} is defined as the 5%-peak cut length along the major axis. respectively, where $\langle \Delta n_x \rangle$ and $\langle \ell_{cut} \rangle$ denotes the averaged value of Δn_x and ℓ_{cut} for each parameter set, respectively. For each N_{pe} data set, X' is scanned from 0.4° to 0.9° in step of 0.1° , corresponding to the points from left to right. Each N_{pe} data set is used to obtain $F_C(N_{pe}, \ell_{cut})$ with the fit to second order polynomial.

The R_P dependence on the angular resolution of n_x ($\sigma(\Delta n_x)$) is obtained in [82] together with the energy dependence on $\sigma(\Delta n_x)$ where $\sigma(\Delta n_x)$ corresponds to the root mean square of the Δn_x distribution. Energy dependence is shown at the fixed R_P of 540 m while the R_P dependence is shown at fixed N_{pe} of 500. On the other hand, clear worsening of the angular resolution proportional to square root of N_{pe} is observed in energy dependence, while a resolution better than 0.1° is obtained with sufficient N_{pe} at higher energies.

After applying the correction function in an event-by-event basis using the calculated ℓ_{cut} and N_{pe} for each “dummy real data” sample, the Δn_x distribution from all parameter sets is obtained as shown in [82]. The resultant angular resolution is estimated to be 0.16° . Considering the fact that N_{pe} for the parameter sets $N_{\text{pe}} = 500$ and the expected N_{pe} from ν_τ signal as discussed in Section 4.3, the geometrical parameters used here would be appropriate to estimate the background contamination since they correspond to the events with less statistical power. This analysis outlines the fact that the high-resolution Cherenkov imaging would lead to the high accuracy reconstruction of the arrival direction, even with the mono detection of Cherenkov showers.

4.7 Background [82]

In this subsection, we evaluate the background events due to air showers. Background events due to the detector itself are discussed in Ref. [8]. Air-shower background candidates are normal cosmic rays, muons, muon neutrinos, τ s, and ν_τ s. From simple flux calculations, it is shown that the neutrino components through mountain, prompt τ components and muons are negligible [86, 87, 88, 89, 90]. Thus, the large zenith angle component of normal cosmic rays is considered as the dominant background component in this study. To simulate this background, CORSIKA is used in the same way as with the ν_τ simulation. To consider the atmospheric depth correctly, “CURVED EARTH” option is selected. The IACT package is used to simulate incoming Cherenkov photons. Protons are selected as the parent particle and a thinning parameter of 10^{-5} is applied. To investigate the zenith angle and the energy dependence of the background flux, a difference in thinning level between this simulation and the ν_τ simulation is unavoidable. The bunch size distribution of the generated showers is studied in this case, too. We find that 74% (93%) of them had 20 (5) bunches or more when detected number of photoelectrons is 40 or more. The applied thinning level of 10^{-5} is acceptable in terms of background estimation precision.

At first, to estimate the background rate during the commissioning observation, the trigger rate for trigger-pixel arrangement adopted in the commissioning observation is calculated. As we could not simulate the largest zenith angle (θ_{zen}) of $\theta_{\text{zen}} > 88^\circ$ in the combination of “CURVED EARTH” and IACT options, trigger pixels are offset by two degrees toward higher elevation to estimate the trigger rate for $88^\circ < \theta_{\text{zen}} < 90^\circ$. To account for the trigger rate decrease due to thicker atmospheric depth, the result is further corrected by the ratio of expected events between $84^\circ < \theta_{\text{zen}} < 86^\circ$ and $86^\circ < \theta_{\text{zen}} < 88^\circ$ in the event that the entire FOV is covered by the trigger pixel. As a result, the number of expected background events (N_{CR}) due to normal cosmic rays during commissioning observation of 197.1 hr is estimated to be:

$$N_{\text{CR}} = 1.3 \times 10^{-4},$$

which is negligible. Note that the above discussion does not use event selection to discard cosmic rays using the reconstructed arrival direction information.

Next, the cosmic-ray background in 1-LC observation with final configuration is evaluated. With the maximum weather efficiency of 100%, 1750 hr of observation time is expected in one year. Assuming a trigger pixel threshold of 20 photoelectrons, which is the same as for our sensitivity estimation, the cosmic-ray shower event rate emerging from the sky region near the mountain edge is found to be 8.2×10^{-2} , 0.55, 4.3, 39 (per year) within 0.1° , 0.3° , 1.0° , 3.0° from the mountain edge, respectively. Assuming perfect reconstruction of the arrival direction, a background-free result is achieved by requiring that the reconstructed direction of the shower axis points back toward the mountain or the Earth because they completely absorb any cosmic-ray secondary particles. In practice, the background-free result will be achieved by requiring a mountain-edge cut in which the reconstructed arrival direction is

inside the mountain edge by θ_{cut} , where θ_{cut} is an angle dependent on the reconstruction accuracy.

The effective aperture with the 3.0° mountain-edge cut is shown [82] to provide estimate the θ_{cut} dependence of the effective aperture, although 3.0° is too large compared with the Ashra-1 angular resolution. The large decrease in the effective aperture at higher energy in the 3.0° mountain-edge cut is due to the fact that higher energy neutrinos could only emerge from the mountain edge because of smaller interaction length. Since larger mountain-edge cut directly affects the effective aperture of the detector, the reconstruction accuracy of the arrival direction is important to realize the background-free observation while keeping a high sensitivity. In addition, it is also very important to positively identify the neutrino shower events. The high-resolution imaging capability would be a key feature in the detection of VHE neutrinos for the first time.

5 Time Frame, Organization, and Funding

At the present time, we are investigating various options for the site, organization, and the design of instruments. Also, we intend to invite other groups to either contribute directly to this project, or to join us on the site with their complementary instruments. The resulting synergy effects would benefit all parties, avoid unnecessary parallel technical developments, and lead to cost savings for the different projects. It is clear that collaboration forming is key to success of the NTA scientific goal. The time frame for the proposed project is thus given both by considerations of budgetary and scientific aspects. In March 19–20, 2014, a preliminary workshop was held at Kashiwa campus of the University of Tokyo to discuss the design of the project and plans with interested colleagues.

We have already set up the International Executive Board (IEB) of NTA for decision making and steering the collaboration since October 12, 2012. Some IEB members have already submitted funding requests to exchange information, detector design, meetings, and construction of the detector. IEB selects the representative who becomes the spokesperson of the collaboration. Each country has a Local Institutional Board (LIB), which is composed of representatives from institutes in the country. LIB selects the representative who becomes a member of IEB. We will set up various Working Groups (WGs) as real working bodies. WG leaders are nominated by LIB and decided by IEB.

Major decisions concerning the hardware implementation should be undertaken in 2014, toward the publication of Project Proposal. In the subsequent two years, components should be developed and tested, and we should continue to request the Japanese government for construction funding. We can eliminate critical developments by using experience from Ashra-1 and NuTel projects. We aim at installing the first detector site and starting commissioning operation in early 2016, if we succeed in the primary Japanese funding in time. We plan to start the operation using at least a part of Site0 and Site1 of proposed four sites by 2018, with the primary construction budget covering at least 1/4 of full operation cost. Once we succeed in the primary funding request and start construction of the first sites, we start the request for matching funds to the governments of various collaborating countries. We aim at starting construction of Site2 and Site3 with the matching funds from countries other than Japan.

Since major choices concerning implementation details are still open at this time, it does not seem appropriate to discuss a detailed cost breakdown. To provide a guideline, however, we have estimated in some detail the cost of one design variant, with major components of the detector either covered by offers from potential manufacturers (light collector mount, mirrors, trigger-readout sensors and electronics, and so on), or extrapolating from well-known costs of the Ashra-1 instruments. On this basis, we estimate the production cost per light

collector in the 20M yen range, plus total R&D costs of about 100M to 150M yen. One detector unit (DU), as shown in Figure 2, requires four light collectors and one trigger and readout unit, so the rough cost estimate is 100M yen per DU. We plan to build at least 12, 6, 6, and 6 DUs at Site0, Site1, Site2, and Site3, respectively, for the coverage of FOV as shown in Table 1, assuming the FOV for DU to be $32^\circ \times 32^\circ$. 30 DUs are needed for covering the total FOV. We do not include infrastructure costs such as site access, site preparation, light collector shelters, networking, and so on. Roughly speaking, at least 100M yen per DU is needed from the experience of the construction of Ashra-1 at Mauna Loa. The current crude estimate is 5000M yen for the construction of NTA.

The Ashra-1 collaboration has agreed to continue the observation at the Mauna Loa site as well as explore the NTA system, at least by the time NTA starts the construction. In order to explore the hardware and software components, the Ashra-1 experience is recognized as an important and useful demonstration of the challenging new detection techniques.

Acknowledgment

We thank P. Binder and J. Goldman from University of Hawaii Hilo for their useful comments and help. Many thanks to the Ashra-1 and NuTel collaborations for their cooperation. The Ashra Experiment is supported by the Coordination Fund for Promoting Science and Technology and by a Grant-in-Aid for Scientific Research from the Ministry of Education, Culture, Sports, Science and Technology of Japan.

References

- [1] M. G. Aartsen et al. *Phys. Rev. Lett.*, 111:021103, Jul 2013.
- [2] C. Kopper. *33rd International Cosmic Ray Conference (<http://www.cbpf.br/icrc2013/>)*, 2013.
- [3] J. Abraham et al. *Phys. Rev. Lett.*, 104:091101, Mar 2010.
- [4] M. Sasaki. *J. Phys. Soc. Jpn.*, 77SB:83, 2008.
- [5] M. Sasaki. *Proc. of ICRR2000 Satellite Symposium: Workshop of Comprehensive Study of the High Energy Universe*, 2000.
- [6] S. Barwick. *Physica Scripta.*, T85:106, 2000.
- [7] Y. Asaoka and M. Sasaki. *Nucl. Instrum. Methods Phys. Res. A*, 647:34, 2011.
- [8] Y. Aita et al. *The Astrophysical Journal Letters*, 736(1):L12, 2011.
- [9] Y. Aita et al. *GCN Circular*, 8632, 2008.
- [10] Y. Asaoka et al. *GCN Circular*, 11291, 2010.
- [11] George WS Hou and MA Huang. *arXiv preprint astro-ph/0204145*, 2002.
- [12] M. Sasaki, A. Kusaka, and Y. Asaoka. *Nuclear Instruments and Methods in Physics Research A*, 492:49–56, October 2002.
- [13] M. Sasaki, Y. Asaoka, and M. Jobashi. *Nuclear Instruments and Methods in Physics Research A*, 501:359–366, April 2003.

- [14] V. Ptuskin, V. Zirakashvili, and E.-S. Seo. *The Astrophysical Journal*, 718(1):31, 2010.
- [15] A. Dar and R. Plaga. *A&A*, 349:259–266, September 1999.
- [16] J. Hinton. *New Journal of Physics*, 11(5):055005, 2009.
- [17] A. Kappes et al. *The Astrophysical Journal*, 656(2):870, 2007.
- [18] F. A. Aharonian et al. *Nature*, 432:75–77, November 2004.
- [19] F. Aharonian et al. *A&A*, 437:L7–L10, July 2005.
- [20] F. Aharonian et al. *Nature*, 439(7077):695–698, 2006.
- [21] F. Aharonian et al. *A&A*, 448:L43–L47, March 2006.
- [22] M. Hoshino, J. Arons, Y. A. Gallant, and A. B. Langdon. *ApJ*, 390:454–479, May 1992.
- [23] D. Horns et al. *A&A*, 451:L51–L54, June 2006.
- [24] F.A. Aharonian et al. *J. Phys. Conf. Ser.*, 39:408, 2007.
- [25] I. F. Mirabel. *Science*, 312:1759, June 2006.
- [26] A. A. Abdo et al. *The Astrophysical Journal*, 688(2):1078, 2008.
- [27] N. Gupta. *Astroparticle Physics*, 48(0):75 – 77, 2013.
- [28] L. A. Anchordoqui et al. *ArXiv e-prints*, June 2013.
- [29] M. Su, T. R. Slatyer, and D. P. Finkbeiner. *The Astrophysical Journal*, 724(2):1044, 2010.
- [30] S. Razzaque. *Phys. Rev. D*, 88:081302, Oct 2013.
- [31] P. Mészáros. *Rep. Prog. Phys.*, 69:2259, 2006. and references therein.
- [32] M. Ackermann et al. *ApJ*, 716(2):1178, 2010.
- [33] J. A. Nousek et al. *ApJ*, 642(1):389, 2006.
- [34] D. Burlon et al. *The Astrophysical Journal Letters*, 685:L19, 2008.
- [35] K. Murase et al. *The Astrophysical Journal Letters*, 651:L5, 2006.
- [36] A. A. Abdo and others (Fermi LAT Coll.). *Astrophys. J. Suppl.*, 183:46, 2009.
- [37] T. Kifune G. Sinnis F.A. Aharonian, J. Buckley. *Rep. Progr. Phys.*, 71:096901, 2008.
- [38] W. Benbow et al. *Proc. 30th Int. Cosmic Ray Conf., Merida, Mexico*, 3:1081, 2007.
- [39] H. Krawczynski et al. *Astrophys. J.*, 601:151, 2004.
- [40] F. Acero H.E.S.S. Coll. et al. *Science*, 326:1080, 2009.
- [41] N. Karlsson et al. *arXiv preprint arXiv:0912.3807*, 2009.
- [42] J. Cosmol A. Loeb, E. Waxman. *Astropart. Phys.*, 0605:003, 2006.
- [43] K. Greisen. *Phys. Rev. Lett.*, 16:748–750, Apr 1966.

- [44] G.T. Zatsepin and V.A. Kuz'min. *JETP Lett.(USSR)(Engl. Transl.)*, 4, 1966.
- [45] V.S. Beresinsky and G.T. Zatsepin. *Physics Letters B*, 28(6):423 – 424, 1969.
- [46] M. Ahlers et al. *Astroparticle Physics*, 34(2):106–115, 2010.
- [47] R.C. Cotta, J.S. Gainer, J.L. Hewett, and T.G. Rizzo. *New Journal of Physics*, 11(10):105026, 2009.
- [48] M. G. Aartsen et al. *Phys. Rev. Lett.*, 110:131302, Mar 2013.
- [49] D.J. Chung, E.W. Kolb, and A. Riotto. *Physical Review D*, 59(2):023501, 1998.
- [50] P. Blasi, R. Dick, and E.W. Kolb. *Astroparticle Physics*, 18(1):57 – 66, 2002.
- [51] I.F.M. Albuquerque, L. Hui, and E.W. Kolb. *Phys. Rev. D*, 64:083504, Sep 2001.
- [52] G. Giacomelli, S. Manzoor, E. Medinaceli, and L. Patrizzii. *Journal of Physics: Conference Series*, 116(1):012005, 2008.
- [53] S.D. Wick, T.W. Kephart, T.J. Weiler, and P.L. Biermann. *Astroparticle Physics*, 18(6):663 – 687, 2003.
- [54] A. De Raújula and S.L. Glashow. *Nature*, 312(5996):734–737, 1984.
- [55] Alexander Kusenko. *Physics Letters B*, 405:108 – 113, 1997.
- [56] S. Kovesi-Domokos G. Domokos. 433:390, 1998.
- [57] A. Letessier-Selvon. *AIP Conf. Proc.*, 566:157, 2000.
- [58] E. Zas H. Athar, G. Parente. *Physical Review D*, 62:093010, 2000.
- [59] D. Fargion. *ApJ*, 570:909, 2002.
- [60] F. Wilczek T. Yu J. Feng, P. Fisher. *Phys. Rev. Lett.*, 88:161102, 2002.
- [61] G. Dalrymple E. Wolfe, W. Wise. *U.S. Geological Survey Professional Paper*, 1557:129, 1997.
- [62] T. Sjöstrand et al. *Comput. Phys. Commun.*, 135:238, 2001.
- [63] S. Agostinelli et al. *Nucl. Instrum. Methods A*, 506:250, 2003.
- [64] S. Iyer Dutta et al. *Physical Review D*, 63:094020, 2001.
- [65] H. Abramowicz and A. Levy. *arXiv:hep-ph/9712415v2*, 1997.
- [66] B. Badelek and J. Kwiecinski. *Rev. Mod. Phys.*, 68:445, 1996.
- [67] S. Jadach et al. *Comput. Phys. Commun.*, 76:361, 1993.
- [68] R. Gandhi et al. *Astropart. Phys.*, 5:81, 1996.
- [69] A. M. Dziewonski and D. L. Anderson. *Physics of the Earth and Planetary Interiors*, 25:297, 1981.
- [70] J.F. Beacom, P. Crotty, and E.W. Kolb. *Phys. Rev. D*, 66:021302, Jul 2002.
- [71] A. Gazizov and M. Kowalski. *Computer physics communications*, 172(3):203–213, 2005.

- [72] R. Gandhi et al. *Physical Review D*, 58:093009, 1998.
- [73] J. Tseng et al. *Physical Review D*, 68:063003, 2003.
- [74] M. Sasaki, Y. Asaoka, and M. Jobashi. *Astropart. Phys.*, 19:37, 2003.
- [75] M. Sasaki. *J. Phys. Soc. Jpn.*, 70(Suppl. B):129, 2001.
- [76] R. Abbasi et al. *Nature*, 484(Supplemental information):351, 2012.
- [77] J. Abraham et al. *Physical Review D*, 79:102001, 2009.
- [78] S. Hümmer, P. Baerwald, and W. Winter. *Phys. Rev. Lett.*, 108:231101, Jun 2012.
- [79] G.J. Feldman and R.D. Cousins. *Physical Review D*, 57(7):3873, 1998.
- [80] R. Abbasi et al. *Phys. Rev. D*, 83:092003, May 2011.
- [81] T.K. Gaisser. High energy neutrinos from space. *arXiv preprint arXiv:1201.6651*, 2012.
- [82] Y. Asaoka and M. Sasaki. *Astroparticle Physics*, 41:7–16, 2013.
- [83] C. Song et al. *Astropart. Phys.*, 14:7, 2000.
- [84] T. Antoni et al. *Astropart. Phys.*, 14:245, 2001.
- [85] R.M. Baltrusaitis et al. *Nucl. Instrum. Methods A*, 240:410, 1985.
- [86] Y. Aita et al. *31th Intl. Cosmic Ray Conf. (Lodz), ID0313*, 2009.
- [87] E. Zas et al. *Astropart.Phys.*, 1:297, 1993.
- [88] R. Enberg et al. *Physical Review D*, 78:043005, 2008.
- [89] A.D. Martin et al. *Acta Physica B*, 34:3273, 2003.
- [90] H. Athar et al. *Astropart.Phys.*, 18:581, 2003.